Chiroptical transmission through a plasmonic helical traveling-wave nanoantenna, towards on-tip chiroptical probes

MENGJIA WANG[1], ROLAND SALUT[1], MIGUEL ANGEL SUAREZ[1], NICOLAS MARTIN[1], AND THIERRY GROSJEAN[1,*]

[1] FEMTO-ST Institute UMR 6174, Univ. Bourgogne Franche-Comte – CNRS – Besancon, France
[*] Corresponding author: thierry.grosjean@univ-fcomte.fr

Compiled September 2, 2019

Resonant plasmonic helices have been widely utilized for locally enhancing and tailoring optical chirality. Here, we investigate their nonresonant operation through the recently introduced concept of plasmonic helical "'traveling-wave"' nanoantenna. Relying on the coupling of a nonresonant plasmonic helix and a nano-aperture, the helical traveling-wave nanoantenna transmit circularly polarized light with the same handedness as the helix and blocks the other, with a measured dissymmetry factor larger than 1.92 (maximum value of 2). This chiroptical transmission is spatially localized, spectrally broadband and background-free. Finally, we demonstrate the possibility to engineer such a plasmonic helical nanoantenna at the apex of a sharp tip typically used in scanning near-field microscopies, thus opening the route for moveable, broadband and background-free chiroptical probes.

http://dx.doi.org/10.1364/ao.XX.XXXXXX

Helical nanoantennas have attracted much interest for enhancing and controlling chiroptical effects, leading to giant circular dichroism [1–3], strongly polarization-dependent transmission [4, 5] and superchiral light [6]. So far plasmonic helices have been designed to be resonant, leading to structures much narrower than the wavelength of the incoming light [4, 6–9]. The operation of resonant nanohelices refers to the "'normal mode"' of radio-wave helical antennas [10, 11]. Such an operation involves deeply subwavelength helices which isotropically scatter light as multipoles, a property also raised at optical frequencies for single nanostructures [7].

When the circumference of a low-frequency helical antenna approaches the vacuum wavelength, its operation is turned into the nonresonant "'axial mode"'[10, 11]. In that regime, helical antennas radiate electromagnetic waves as circularly polarized directional beams propagating along the helix axis. Recently, the axial mode has been demonstrated at optical frequencies onto a subwavelength plasmonic helix, leading to the concept of helical travelling-wave nanoantenna (HTN) [12]. As its low-frequency counterpart, the HTN belongs to the family of nonresonant "'travelling-wave"' optical antennas [13–16]. This nanoantenna results from the combination of an individual plasmonic helix and a light reflector (here a gold surface), the helix being end-fired with the localized plasmon mode of a nano-aperture perforated right at the helix pedestal. HTNs have shown new degrees of freedom in the control of light polarization [12].

In this letter, we address the dissymmetric transmission response of the nanoantenna to right and left-handed circularly polarized incoming waves, a phenomenon defined as chiroptical transmission. We evidence that an individual left-handed HTN transmits light of left circular polarization and blocks the other. A chiroptical transmission contrast Δ larger than 0.96 (dissymmetry factor g of 1.92) [2, 5] is measured for wavelengths ranging from 1.47 to 1.65 μm. The numerically predicted value of Δ remains larger than 0.99 for wavelengths ranging from 1.48 to 1.7 μm. So far most research has focused on plasmonic helical nanoantennas fabricated on planar substrates, thus restricting their applications. We finally demonstrate the feasibility of an individual HTN (and by extension plasmonic helix) at the apex of a tip used in scanning near-field microscopy. This opens the route for moveable chiroptical probes featuring spectrally broadband and background-free operation.

We fabricated individual carbon-gold core-shell helices [5] designed to operate in the nonresonant axial mode at telecommunication wavelengths (λ around 1.55 μm). The carbon helical skeleton is sculpted by focused ion beam induced deposition (FIBID) [17]. Metal coating is realized by sputter-depositing a thin layer of gold onto the carbon core with a metal target tilted with an angle of 80° from the helix axis and rotated during the deposition time with a constant rotating speed of 2 rev.min^{-1}. We combined these two techniques to fabricate plasmonic helices consisting of a 105-nm diameter carbon wire wound up in the form of a four-turn corkscrew-type structure and covered with a 25-nm thick gold layer. The resulting helix has a 505-nm outer diameter and is 1.66-μm high. It is positioned on a cylindrical pedestal of 105 nm diameter and 100 nm high carbon whose lateral side is also coated with a 25-nm thick gold layer. Note that the resulting subwavelength structure fulfills the geometrical requirement of low-frequency helices for operation in the nonresonant axial mode [10, 11], i.e., its outer circumference equal to

1585 nm matches the targeted telecommunication wavelengths.

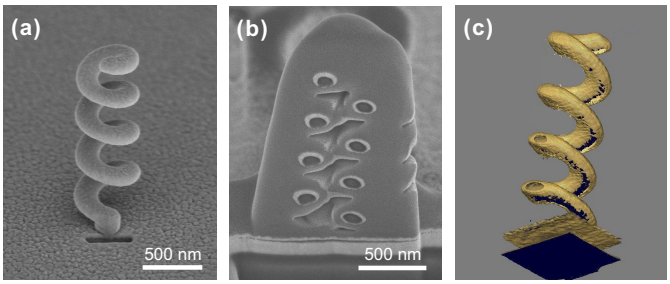

Fig. 1. (a) Scanning electron micrograph of a HTN which combines a nonresonant gold-coated carbon helix coupled to a rectangle nanoaperture. (b) Scanning electron micrograph of a cross-section of the helix initially embedded in platinum by FIBID. (c) Reconstructed 3D image of the fabricated gold-coated carbon helix via FIB/SEM tomography of the platinum embedded nanostructure. Yellow: gold; black: carbon.

We considered this plasmonic helix as a part of a HTN. To this end, the core-shell structure is engineered onto a 100-nm thick gold layer deposited onto a glass substrate and a 370 nm-by-40 nm rectangle nano-aperture is engraved by focused ion beam (FIB) milling in the flat gold layer right at the helix pedestal (Fig. 1(a)). To evaluate the thickness of the gold layer deposited onto the helical carbon core, we perform tomography of the helix by alternating FIB slicing and SEM imaging of the nanostructure. To this end, the helix is embedded in platinum deposited by FIBID. We see in the helix cross-section of Fig. 1(b) that the gold layer (white rings in the image) is not homogeneously distributed all around the carbon wire (dark circular regions in the SEM image). Figure 1(c) shows a 3D reconstruction of the gold-coated carbon helix revealing a bottom side that is not fully covered with gold. The tilt angle of the gold target of 80° creates a little shadowing effect in the gold coating process which prevents uniform gold layer to be deposited all around the helical wire. Inhomogeneous metal coating around the carbon core may spectrally redshift the helix optical response, as already observed in Ref. [12].

We performed three-dimensional FDTD simulations using commercial software (Fullwave). The antenna is modeled as a wounded cylindrical carbon wire coated with a 25-nm thick gold layer. The helix is placed next to a rectangle aperture in an extended gold slab lying on a glass substrate. The geometrical parameters of the simulated HTN are those of the structure introduced above. The non-uniform meshgrid within the computation volume varies from 30 nm for portions at the periphery of the simulation to 5 nm within and near the helix and the aperture nanoantenna. The helix is illuminated with a circularly polarized gaussian beam (beam waist: 2.3 μm) propagating along the helix axis. We calculated the transmitted light through the nano-aperture in the substrate for two incoming circular polarizations of opposite handedness. An overview is shown in Fig. 2(a). The antenna response at λ=1.57 μm is reported in Figs. 2 (b) and (c) for the left and right circular polarizations, respectively.

The HTN used in collection mode shows a dissymmetric transmission response regarding the right and left circular polarization states (Fig. 2 (b) and(c)).At λ=1.57 μm, 17% and 0.04% of the incoming power are transmitted through the HTN for incoming left and right circular polarizations, respectively. To quantify such an unbalanced response to the polarization handedness, we used the chiroptical transmission contrast $\Delta = (T_{LCP} - T_{RCP})/(T_{LCP} + T_{RCP})$ and related dissymmetry factor $g = 2\Delta$ [5]. T_{LCP} and T_{RCP} are the power transmission spectra of the HTN used in light collection mode for incoming right and left circular polarizations, respectively. Figure 2 (d) reports on a calculated chiroptical transmission contrast peaking at 1 ($g = 2$) when λ=1.57 μm and remaining larger than 0.99 for wavelengths ranging from 1.48 to 1.7 μm. Simulations thus predict an extreme chiroptical transmission contrast of the HTN over a broad spectral bandwidth.

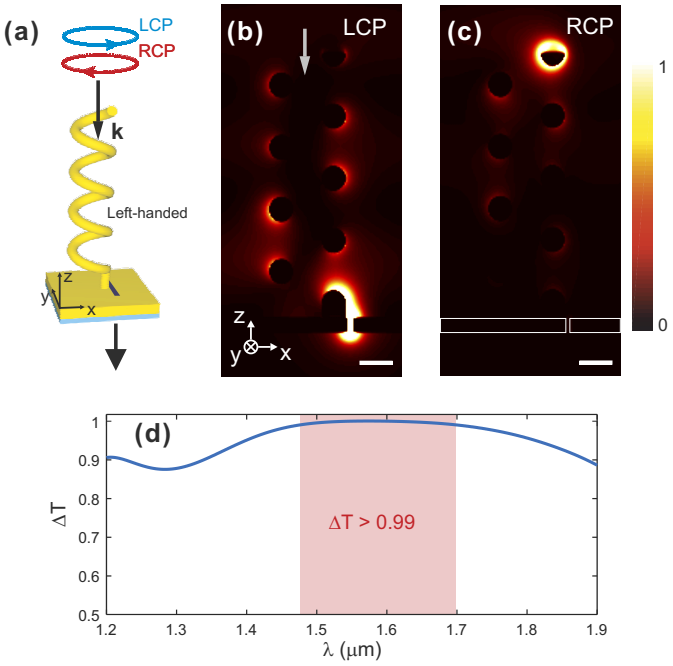

Fig. 2. (a) Description of the numerical study with the FDTD method. A focused beam is projected onto the helix. The two right and left circular polarizations are considered in two distinct simulations. (b) and (c) Intensity cross-section of the HTN in the (x0z)-plane with incoming right and left circular polarizations, respectively (λ=1.57 μm). Scale bars: 200 nm. (d) Spectrum of the chiroptical transmission contrast Δ of the HTN used in collection mode (simulations in pulsed regime followed by Fourier transform). The dissymmetry factor g [2, 5] can be simply deduced by doubling Δ.

To experimentally verify the chiroptical transmission properties of a HTN, we characterized the power transfer through the nanoantenna both in the radiation and collection modes represented in Fig. 3 (a). To this end, linearly polarized light from a tunable laser (Yenista) passes through a rotating quarter-wave plate (QWP; AHWP05M-1600, Thorlabs) before being focused with a (25X, 0.4) microscope objective onto the HTN. The quarter-wave plate is mounted onto a motorized stage (PRM1Z8, Thorlabs) to be accurately rotated with respect to the incident linear polarization direction. The light transmitted through the nanoantenna is detected by imaging the plasmonic structure with an (50X, 0.65) infrared objective from Olympus coupled to an infrared camera (GoldEye model G-033, Allied Vision Technologies GmbH). In the radiation and collection modes of the HTN, the rectangle nano-aperture and the helix are selectively illuminated, respectively. In Fig. 3 (b) the spectra are obtained by studying the nanoantenna transmission as a function of the

wavelength of the incoming light. At each wavelength, the transmitted intensity is measured for two orthogonal orientations of the quarter-wave plate leading to circular right and left polarizations (fast axis of the waveplate at $\pm\pi/4$ relative to the incident polarization direction). Then, the chiroptical transmission contrast Δ and dissymmetry factor g are deduced from these measurements.

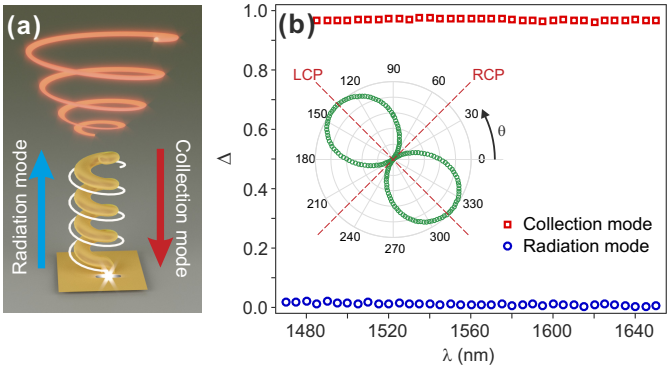

Fig. 3. (a) Schematics of the two experimentally investigated operations of the HTN, involving light wave propagation in two opposite directions along the helix axis. The collection mode of interest involves helix illumination (red arrow) whereas the radiation mode implies aperture illumination from the backside (blue arrow). (b) Experimental spectra of the chiroptical transmission contrast Δ in both the radiation and collection modes of the HTN. Figure inset: transmitted signal (normalized value) through the HTN used in collection mode at λ=1.55 μm, as a function of the incoming polarization (i.e., the angle θ between the fast axis of the rotating quarter-wave plate and the direction of the incoming linear polarization).

We see that Δ is almost equal to zero in the radiation mode of the HTN. This can be easily explained by the dipolar nature of the rectangle nano-aperture which imposes a linearly polarized end-firing of the plasmonic helix regardless of the incoming polarization. The nano-aperture acts as a nanoscale linear polarization filter. In collection mode, Δ remains larger than 0.96 (g larger than 1.92) over the whole spectral bandwidth of the laser. This result agrees well with the numerical predictions in Fig. 2. It confirms that the HTN develops a strongly dissymmetric transmission response to right and left circular polarizations when used in collection mode. We also measure the light transmitted by the HTN while rotating the quarter-wave plate by one turn. The typical two-lobe pattern of the resulting diagram evidences a $\cos^2(\theta + \pi/4)$ dependence of the detected signal, where θ is the angle between the quarter-wave plate and the linear polarizer. Right and left circular polarizations are obtained for $\theta = \pi/4$ and $\theta = -\pi/4$, respectively. This signifies that the right-handed circular component of all incoming polarization states are filtered out by the HTN in its transmission process. The HTN thus blocks the optical waves whose handedness is opposite to the helix, regardless the incoming polarization. The nanoantenna thus acts as a local circular analyzer.

So far most research has focused on plasmonic helical nanoantennas fabricated on planar substrates, thus restricting their applications. We finally investigate the possibility to integrate an individual HTN at the apex of the sharp tips used in scanning near-field microscopy. To this end, we considered a typical

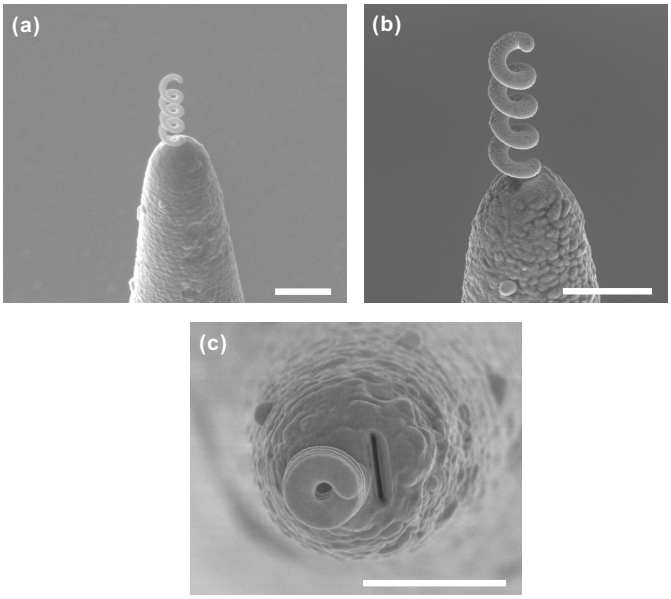

Fig. 4. HTN at the apex of a tip used in scanning near-field microscopy. (a) Large view of the helix carbon skeleton sculpted by FIBID at the very tip. (b) On-tip gold-coated carbon helix. (c) Finalized HTN after the FIB milling of a rectangle nano-aperture in contact to the helix pedestal. Scale bars: 1 μm.

model of a sharp dielectric near-field tip. The tip was covered with a 100-nm thick layer of aluminum. Then, the two-step fabrication of the carbon-gold core-shell helix is carried out. Finally, a rectangle nano-aperture is engraved in the tip metal-coating, right at the helix pedestal. Figure 4 shows three SEM images of the on-tip structure after the three fabrication steps of the HTN. Changing the holder does not affect much the HTN fabrication. FIBID keeps its high level of accuracy in the definition of the helix geometry and metal coating still leads to smooth gold layers compatible with plasmonics. This fabrication process covers apertureless plasmonic traveling-wave helices and may be extended to the on-tip engineering of individual resonant helices. In the case of tips with nanoscale apex such as those used in atomic force microscopy (AFM), a flat of 200-400nm width could be engineered by FIB at the very tip prior to FIBID to ensure a reliable fabrication process of the helices. Apertureless HTNs would then be privileged.

To conclude, we investigate the chiroptical transmission through a HTN. We numerically and experimentally show a highly dissymmetric light transmission through the nanoantenna for incoming right and left circular polarizations. Relying on a nonresonant plasmonic helix coupled to a nanoaperture in an opaque metal film, the HTN combines a high chiroptical transmission contrast over a broad spectral bandwidth and a background-free operation. We finally show the feasibility of an individual HTN at the apex of a tip used in scanning near-field optical microscopy, opening the route for moveable, broadband and background-free chiroptical probes. Tip-integrated plasmonic helices could be useful to locally probe light helicity [18, 19], optical chiral effects and enantioselective optical forces (when an AFM tip is used) [20]. Owing to their well-defined coil shape, non-resonant plasmonic helices may be appealing devices for tailoring opto-mechanic, opto-acoustic and magneto-optic phenomena. On-tip fabrication of resonant helices may also be possible. Coupling resonant helices to coaxial nanoapertures

[21, 22] would enable for instance background-free chiral-dipole probes.

FUNDING

Region Bourgogne Franche-Comte; EIPHI Graduate School (ANR-17-EURE-0002); Agence Nationale de la Recherche: ANR-18-CE42-0016

REFERENCES

1. J. Gibbs, A. Mark, S. Eslami, and P. Fischer, Appl. Phys. Lett. **103**, 213101 (2013).
2. M. Esposito, V. Tasco, M. Cuscuna, F. Todisco, A. Benedetti, I. Tarantini, M. D. Giorgi, D. Sanvitto, and A. Passaseo, ACS Photon. **2**, 105 (2014).
3. M. Esposito, V. Tasco, F. Todisco, M. Cuscunà, A. Benedetti, D. Sanvitto, and A. Passaseo, Nat. Commun. **6**, 6484 (2015).
4. J. K. Gansel, M. Thiel, M. S. Rill, M. Decker, K. Bade, V. Saile, G. von Freymann, S. Linden, and M. Wegener, Science. **325**, 1513 (2009).
5. D. Kosters, A. De Hoogh, H. Zeijlemaker, H. Acar, N. Rotenberg, and L. Kuipers, ACS photonics **4**, 1858 (2017).
6. M. Schäferling, X. Yin, N. Engheta, and H. Giessen, ACS Photonics **1**, 530 (2014).
7. P. Wozniak, I. De Leon, K. Hoeflich, C. Haverkamp, S. Christiansen, G. Leuchs, and P. Banzer, Opt. Express **26**, 19275 (2018).
8. P. Woźniak, I. De León, K. Höflich, G. Leuchs, and P. Banzer, Optica **6**, 961 (2019).
9. K. Höflich, T. Feichtner, E. Hansjürgen, C. Haverkamp, H. Kollmann, C. Lienau, and M. Silies, Optica **6**, 1098 (2019).
10. C. Balanis, *Antenna theory: analysis and design* (John Wiley & Sons, New-York, 1997).
11. J. D. Kraus, R. J. Marhefka, and A. S. Khan, *Antennas and wave propagation* (Tata McGraw-Hill Education, 2006).
12. M. Wang, R. Salut, H. Lu, M.-A. Suarez, N. Martin, and T. Grosjean, Light. Sci. Appl. **8**, 1 (2019).
13. Y. Wang, A. S. Helmy, and G. V. Eleftheriades, Opt. Express **19**, 12392 (2011).
14. M. Peter, A. Hildebrandt, C. Schlickriede, K. Gharib, T. Zentgraf, J. Forstner, and S. Linden, Nano Lett. **17**, 4178 (2017).
15. F. Monticone and A. Alu, Proc. IEEE **103**, 793 (2015).
16. X.-X. Liu and A. Alù, Phys. Rev. B **82**, 144305 (2010).
17. M. Esposito, V. Tasco, F. Todisco, M. Cuscunà, A. Benedetti, M. Scuderi, G. Nicotra, and A. Passaseo, Nano Lett. **16**, 5823 (2016).
18. S. Hashiyada, T. Narushima, and H. Okamoto, ACS Photonics **5**, 1486 (2018).
19. L. Sun, B. Bai, J. Wang, M. Zhang, X. Zhang, X. Song, and L. Huang, Adv. Funct. Mater. p. 1902286 (2019).
20. Y. Zhao, A. A. Saleh, M. A. Van De Haar, B. Baum, J. A. Briggs, A. Lay, O. A. Reyes-Becerra, and J. A. Dionne, Nat. Nanotechnol. **12**, 1055 (2017).
21. P. Banzer, J. Kindler, S. Quabis, U. Peschel, and G. Leuchs, Opt. Express **18**, 10896 (2010).
22. F. I. Baida, Appl. Phys. B **89**, 145 (2007).

REFERENCES

1. J. Gibbs, A. Mark, S. Eslami, and P. Fischer, "Plasmonic nanohelix metamaterials with tailorable giant circular dichroism," Appl. Phys. Lett. **103**, 213101 (2013).
2. M. Esposito, V. Tasco, M. Cuscuna, F. Todisco, A. Benedetti, I. Tarantini, M. D. Giorgi, D. Sanvitto, and A. Passaseo, "Nanoscale 3d chiral plasmonic helices with circular dichroism at visible frequencies," ACS Photonics **2**, 105–114 (2014).
3. M. Esposito, V. Tasco, F. Todisco, M. Cuscunà, A. Benedetti, D. Sanvitto, and A. Passaseo, "Triple-helical nanowires by tomographic rotatory growth for chiral photonics," Nat. Commun. **6**, 6484 (2015).
4. J. K. Gansel, M. Thiel, M. S. Rill, M. Decker, K. Bade, V. Saile, G. von Freymann, S. Linden, and M. Wegener, "Gold helix photonic metamaterial as broadband circular polarizer," Science. **325**, 1513–1515 (2009).
5. D. Kosters, A. De Hoogh, H. Zeijlemaker, H. Acar, N. Rotenberg, and L. Kuipers, "Core–shell plasmonic nanohelices," ACS photon. **4**, 1858–1863 (2017).
6. M. Schäferling, X. Yin, N. Engheta, and H. Giessen, "Helical plasmonic nanostructures as prototypical chiral near-field sources," ACS Photonics **1**, 530–537 (2014).
7. P. Wozniak, I. De Leon, K. Hoeflich, C. Haverkamp, S. Christiansen, G. Leuchs, and P. Banzer, "Chiroptical response of a single plasmonic nanohelix," Opt. Express **26**, 19275–19293 (2018).
8. P. Woźniak, I. De León, K. Höflich, G. Leuchs, and P. Banzer, "Interaction of light carrying orbital angular momentum with a chiral dipolar scatterer," Optica **6**, 961 (2019).
9. K. Höflich, T. Feichtner, E. Hansjürgen, C. Haverkamp, H. Kollmann, C. Lienau, and M. Silies, "Resonant behavior of a single plasmonic helix," Optica **6**, 1098–1105 (2019).
10. C. Balanis, *Antenna theory: analysis and design* (John Wiley & Sons, New-York, 1997).
11. J. D. Kraus, R. J. Marhefka, and A. S. Khan, *Antennas and wave propagation* (Tata McGraw-Hill Education, 2006).
12. M. Wang, R. Salut, H. Lu, M.-A. Suarez, N. Martin, and T. Grosjean, "Subwavelength polarization optics via individual and coupled helical traveling-wave nanoantennas," Light. Sci. Appl. **8**, 1–8 (2019).
13. Y. Wang, A. S. Helmy, and G. V. Eleftheriades, "Ultra-wideband optical leaky-wave slot antennas," Opt. Express **19**, 12392–12401 (2011).
14. M. Peter, A. Hildebrandt, C. Schlickriede, K. Gharib, T. Zentgraf, J. Forstner, and S. Linden, "Directional emission from dielectric leaky-wave nanoantennas," Nano Lett. **17**, 4178–4183 (2017).
15. F. Monticone and A. Alu, "Leaky-wave theory, techniques, and applications: from microwaves to visible frequencies," Proc. IEEE **103**, 793–821 (2015).
16. X.-X. Liu and A. Alù, "Subwavelength leaky-wave optical nanoantennas: Directive radiation from linear arrays of plasmonic nanoparticles," Phys. Rev. B **82**, 144305 (2010).
17. M. Esposito, V. Tasco, F. Todisco, M. Cuscunà, A. Benedetti, M. Scuderi, G. Nicotra, and A. Passaseo, "Programmable extreme chirality in the visible by helix-shaped metamaterial platform," Nano Lett. **16**, 5823–5828 (2016).
18. S. Hashiyada, T. Narushima, and H. Okamoto, "Imaging chirality of optical fields near achiral metal nanostructures excited with linearly polarized light," ACS Photonics **5**, 1486–1492 (2018).
19. L. Sun, B. Bai, J. Wang, M. Zhang, X. Zhang, X. Song, and L. Huang, "Probing the photonic spin–orbit interactions in the near field of nanostructures," Adv. Funct. Mater. p. 1902286 (2019).
20. Y. Zhao, A. A. Saleh, M. A. Van De Haar, B. Baum, J. A. Briggs, A. Lay, O. A. Reyes-Becerra, and J. A. Dionne, "Nanoscopic control and quantification of enantioselective optical forces," Nat. Nanotechnol. **12**, 1055 (2017).
21. P. Banzer, J. Kindler, S. Quabis, U. Peschel, and G. Leuchs, "Extraordinary transmission through a single coaxial aperture in a thin metal film," Opt. Express **18**, 10896–10904 (2010).
22. F. I. Baida, "Enhanced transmission through subwavelength metallic coaxial apertures by excitation of the tem mode," Appl. Phys. B **89**, 145–149 (2007).